Applied Energy 237 (2019) 695–707

Contents lists available at ScienceDirect

Applied Energy

journal homepage: www.elsevier.com/locate/apenergy

Optimal operational planning of scalable DC microgrid with demand response, islanding, and battery degradation cost considerations

Muhammad Fahad Zia[a], Elhoussin Elbouchikhi[b], Mohamed Benbouzid[a,c,*]

[a] University of Brest, UMR CNRS 6027 IRDL, 29238 Brest, France
[b] ISEN Brest, Yncréa Ouest, UMR CNRS 6027 IRDL, 29200 Brest, France
[c] Shanghai Maritime University, 201306 Shanghai, China

HIGHLIGHTS

- Regression models to determine temperature and DOD effects on Li-ion battery degradation.
- Practical Li-ion battery degradation cost model using regression models.
- Practical PV system LCOE for hot and cold climate regions using real temperature and irradiance data.
- Incentive-based demand response to encourage customers changing their consumption patterns.
- Power flow inclusion in the optimization model to regulate bus voltages and compute system losses.

ARTICLE INFO

Keywords:
DC microgrid
Photovoltaic system
Li-ion battery
Battery degradation cost model
Demand response
Energy management system
Optimization

ABSTRACT

With the advancements in power electronic devices, the increasing use of DC loads, DC renewable generation sources and battery storage systems, and no reactive power and frequency stability issues, DC microgrids are increasingly gaining attention in both academia and industry. In this paper, a grid-connected DC microgrid is considered, which consists of a PV system and a Li-ion battery. DC microgrids optimal operation requires battery degradation cost modeling and demand response incentive for active consumers' participation to be addressed in detail. Therefore, a practical degradation cost model for a Li-ion battery is developed to optimize battery scheduling and achieve its realistic operational cost. Apart from energy price, scheduled islanding responsive demand response incentive is also introduced to encourage customers to shift load during scheduled grid-tie line maintenance. Levelized cost of energy of PV system is calculated for both hot and cold climate regions. Optimal operation of DC microgrid cannot be achieved without considering nodal voltages and system losses. Hence, network constraints are also included in the proposed model. Extensive numerical simulations are carried out to prove the effectiveness of the proposed approach. The achieved results would aid in DC microgrids adoption planning that would expectedly replace traditional AC grids in the future.

1. Introduction

Renewable energy sources (RESs) are being deployed on a large scale due to the advancement and maturity in their technologies. Among these sources, photovoltaic (PV) systems are leading in terms of installation and utilization followed by wind turbines. Integration of these sources along with energy storage systems paves the way for microgrids (MGs) [1]. An MG integrates all such distributed energy sources with plug and play ability to operate in islanded mode during maintenance or failure of grid-tie line [2]. MGs reduce burden on aging transmission network by meeting load demand locally with the help of distributed energy sources connected to local substation and distribution networks [3,4].

MGs can be either AC or DC, and hybrid depending upon the type of buses, loads, and RESs [5,6]. Although, current utility grid (UG) system is of AC type, DC loads such as lightening systems, computers, and battery chargers are significantly increasing [7]. Recent advancements in power electronic devices also pave the way for modeling loads as constant power loads due to negligible effects of transient behavior in output power of many loads [8]. Moreover, quite a few RESs produce

* Corresponding author.
E-mail addresses: muhammadfahad.zia@univ-brest.fr (M.F. Zia), elbouchikhi@isen-bretagne.fr (E. Elbouchikhi), mohamed.benbouzid@univ-brest.fr (M. Benbouzid).

https://doi.org/10.1016/j.apenergy.2019.01.040
Received 22 October 2018; Received in revised form 23 December 2018; Accepted 4 January 2019
Available online 14 January 2019
0306-2619/

Nomenclature

χ_d^{Υ}	depth of discharge dependent battery cyclelife factor
χ_T^{Υ}	temperature dependent battery cyclelife factor
χ_T^{Ξ}	temperature dependent battery capacity factor
Δt	time interval
$\delta_1, \delta_2, \delta_3$	time-of-use based scaling factors for demand response incentives
η^{ch}	charging efficiency of battery
η^{dch}	discharging efficiency of battery
$\mathcal{N}_{\mathcal{V}}, \mathcal{N}_{\mathcal{W}}, \mathcal{N}_{\mathcal{X}}$	sets of PV, battery, and load buses
$\mathcal{N}$	set of all buses including grid bus
$\mathcal{T}_1, \mathcal{T}_2, \mathcal{T}_3, \mathcal{T}$	sets of off-peak, mid-peak, on-peak, and all time slots
$\mathcal{T}_{sh}$	set of forward and backward shifting time instants
Φ	chemical reaction rate of Li-ion battery
Φ_{ref}	chemical reaction rate of Li-ion battery at reference temperature
π_t^{dr}	demand response incentive price at time t
π_t^{g+}, π_t^{g-}	buying and selling electricity prices at time t
ρ_1, ρ_2, ρ_3	schedlued islanding sensitive scaling factors for demand response incentives
σ	PV system degradation factor
$\Upsilon_{w,ref}$	reference cyclelife of Li-ion battery at battery bus w
$\Xi_{w,ref}$	rated energy capacity of Li-ion battery at battery bus w
$\Xi_{w,t}$	Li-ion battery energy capacity at battery bus w and time t
C^b, C^b_{inv}, C^b_{om}	battery degradation, investment, and operation and maintenance costs
C^b_{inv}	investment cost of battery
$C^{pv}, C^{pv}_{inv}, C^{pv}_{om}$	levelized cost, investment cost, and operation and maintenance cost of PV system
C^{voll}	value of lost load
CR_{max}	maximum charging (discharging) rate limit of Li-ion battery
d	depth of discharge of Li-ion battery
dr	discount rate
E^{pv}_{an}	annual energy produced by PV system
$E_a(\Phi)$	activation energy
G_t	irradiance at time t
G_{NOCT}	irradiance at PV array nominal operating cell temperature
G_{STC}	irradiance at PV array standard test conditions
$h_{\Upsilon}(d), h_{\Upsilon}(T)$	regression model for battery cyclelife dependence on depth of discharge and temperature
$h_{\Xi}(T)$	regression model for battery capacity dependence on temperature
L^b_{ref}	battery cyclelife at reference conditions
L^b_t	baseline power demand at time t
N^{pv}	number of PV arrays
$NOCT$	nominal operating cell temperature
P^i_t	active power at bus i during time t
$P^{ch}_{w,t}$	charging power of battery at battery bus w and time t
$P^{dch}_{w,t}$	discharging power of battery at battery bus w and time t
$P^{dr+}_{x,t}$	power demand at load bus x shifted from time t
$P^{dr-}_{x,t}$	power demand at load bus x shifted at time t
$P^{DR}_{i,t}$	maximum shiftable power demand from period t
$P^{dr}_{x,i,t}$	power demand at bus x shifted from time slot i to t
P^{g+}_t, P^{g-}_t	buying and selling power from/to grid power at time t
P^{loss}_t	power loss of the DC microgrid system at time t
$P^{loss}_{ij,t}$	line loss of branch connected between bus i and bus j
$P^{ls}_{x,t}$	power demand of lost load at load bus x and time t
P^{l}_t	power demand at time t after shifting
P^{pv}_{STC}	PV array power output at standard test conditions
$P^{pv}_{v,t}$	power output of PV system at PV bus v and time t
R	gas constant
$R^{ch}_{w,t}$	charging rate of Li-ion battery at battery bus w and time t
$R^{dch}_{w,t}$	discharging rate of Li-ion battery at battery bus w and time t
RV	residual value of Li-ion battery
T	ambient temperature
t	indices of time slots
t_f	end time
t_s	start time
T_c	cell temperature of PV array
T_{ref}	reference temperature
T_{STC}	cell temperature of PV array at standard test conditions
v, w, x	indices of PV, battery, and load buses
V^i_t	voltage at bus i during time t
V^i_{max}	maximum limit of bus voltage
V^i_{min}	minimum limit of bus voltage
y_{ij}	line admittance from bus i to bus j
z_t	islanding status at time t

DC voltages, thus requiring power converters for AC conversion that reduces efficiency of the overall system. DC MGs are less complex power systems with the advantages of no reactive power flow and no complex control circuitry for frequency stability as well [9]. DC MGs can operate in grid-connected and islanded modes.

The battery storage system plays a vital role in an MG as it can be used in various applications such as peak demand management, uncertainties handling caused by RESs, and providing supply to load end during islanding operation [10,11]. In DC MG operation, battery continuously charges and discharges, which affects its performance and cyclelife. Hence, a practical model of battery degradation cost (BDC) is necessary to optimize its scheduling during DC MG operation. Battery performance is affected by charge (discharge) rate, depth of discharge (DOD), state of charge (SOC), and temperature. Therefore, BDC should be modeled considering all these parameters. Such BDC model avoids higher costs for the DC MG operator (DMO) due to imprudent charging and discharging times.

Researches have proposed various BDC models for battery scheduling optimization and overall system operation. An economic operation of a PV/battery system with a basic BDC model was proposed in [12]. However, the BDC model has not included explicit consideration of battery aging factors, thus providing inefficient cost-competitive model. In [13], a PV/battery system has scheduled its decision strategies using operating cost model that considers only capacity fading effects in modeling BDC. Moreover, battery degradation model was used in energy management of remote MGs in [14]. The degradation model considers DOD effects on battery lifetime only. The other battery aging factors are not taken into consideration. In [15], an optimized management of PV integrated off-grid power system was achieved. MG energy scheduling was achieved by using only DOD-dependent BDC model in operational cost-function of MG [16]. The BDC model was developed by considering only lifetime energy throughput of battery and ignoring other aging factors.

A grid-connected PV/battery system operation was proposed in [17]. In this study, DOD-dependent battery cyclelife degradation model estimates battery sizing. However, the daily rule-based operation neglects battery degradation in deciding strategies for efficient PV/battery system operation. Rule and model predictive-based control techniques were used to minimize the operating cost of PV/battery system in [18]. The developed model includes capacity loss degradation in battery operation that considers only SOC-based aging effects. Moreover, the degradation cost of battery is hypothetically assumed. Authors in [19] have proposed battery aging model for MG optimal design. The degradation model is developed based on capacity loss of battery that

considers capacity fading only. Moreover, the capacity loss is taken constant for a range of temperature without providing reference of any manufacturers datasheet. Operating cost of RESs-based MG is optimized in [20]. Authors have considered only the DOD related aging effects in BDC modeling, which does not provide the practical degradation model for batteries. All these battery degradation models only consider capacity fading of battery, while ignoring power fading. Capacity fading is related to cyclelife degradation of battery and power fading is related to ohmic and reaction losses, which is connected to energy (discharged) capacity degradation of battery. Optimal operation of battery in a DC MG is a complex problem due to its intertemporal nature. Lead acid and Li-ion batteries are the most widely used energy storage systems in energy management applications. Nowadays, Li-ion batteries are dominating due to their high energy density, no memory effect, and increased resistance to temperature effects. They are being deployed at large scale for utility, regulation, and electric vehicle (EV) applications [21]. In 2017, annual deployment of Li-ion batteries was 2 GWh, and it is predicted to go up to 18 GWh in 2022 [22]. In this paper, BDC of a Li-ion battery is modeled to optimize the overall operation of a DC MG.

Demand response (DR) is becoming an integral part of power system and MGs due to its applications in minimizing system operational cost [23], congestion management [24], peak demand management [25], defer investment in power network [26], system reliability [27], and ancillary services [28]. DR operation is achieved by utilizing smart meters, advanced metering infrastructure, and energy information systems. An advanced metering infrastructure is used to collect data from metering devices using home area network. These data log are sent to service provider by wide area network for analysis in order to achieve energy cost and consumer service optimization [29].

DR is divided mainly into two types, price-based DR (PDR) and incentive-based DR (IDR). PDR programs help the consumers to change their consumption pattern with time-varying energy prices. However, IDR programs provide benefits to consumers for reducing their load demand following DR requests. Most utilities provides PDR programs to their consumers instead of IDR, but PDR shares a small contribution in overall DR resource base [30]. IDR provides great provision and control to DMO, which enables performing efficient MG operation. In this paper, IDR is used for optimal and efficient operation of a DC MG.

A generalized PV and battery-based grid-connected DC MG model is presented in Fig. 1. PV system, and DC and AC loads are connected to the DC network through DC/DC converters and inverters, respectively. A bidirectional DC/DC converter is used to control power flow between Li-ion battery and DC network during charging and discharge. In grid-connected mode, a DC MG can reap advantages of selling power to UG during excess supply period and the bidirectional DC/AC converter is used for this purpose. While in islanded mode, it provides supply to loads through local sources. All the energy sources, loads, and UG local controllers communicate with each other and DMO using communication technologies. These wired and wireless technologies are selected based on the criteria of deployment cost, coverage area, and data rate [1]. Power output of the PV system is used at first to meet load demand followed by UG power and battery power. DMO needs centralized decision-making strategies to avoid ineffective and costly operation of the DC MG. Therefore, optimized daily scheduling of energy sources in a DC MG requires an energy management model to minimize its operating cost and optimize its daily operation.

In this paper, optimal operation of a scalable PV and Li-ion battery based grid-connected DC MG is studied considering scheduled islanding and time-of-use (TOU) based IDR schemes. The BDC model of Li-ion battery is developed taking into account the effects of temperature and DOD on battery performance. The levelized cost of energy (LCOE) of the PV system is determined using real data of temperature and irradiance of hot and cold weather climate regions, namely Dammam (Saudi Arabia) and Brest (France), respectively. The proposed cost-operation model of a scalable grid-connected DC MG is a nonlinear programming model that also considers bus voltages and includes system losses in power balance constraint. The contributions of this paper can be summarized as follows:

- Regression models are developed to determine temperature and DOD effects on cyclelife and energy capacity degradation of a Li-ion battery.
- A practical BDC model of Li-ion battery is presented using the developed regression models.
- A practical LCOE of a PV system for hot and cold climate regions is computed using real temperature and irradiance data.
- An IDR is introduced to encourage customers to change their consumption patterns during normal operation.
- An islanding responsive IDR is proposed to encourage customers to shift load from scheduled islanding periods to normal operation periods.
- Power flow of a scalable DC MG system is also included in the optimization model to regulate bus voltages and compute system losses.

2. Battery degradation modeling

Li-ion battery energy storage systems are an essential part of MGs due to their high power and energy densities, good cyclelife, and improved efficiency. They are being widely used in energy systems for various applications such as bulk storage, peak shaving, frequency regulation, voltage support, reserve capacity, and transmission and distribution deferral [31]. Nowadays, Li-ion batteries are the most mature and commercial technologies used in power system. However, integration of Li-ion battery into an MG system requires its degradation cost-modeling for effective and efficient operation.

Increasing cell impedance and decreasing battery capacity due to unwanted side reactions lead to fast degradation of battery [32,33]. Hence, the battery chemistry and its scheduling operation plays a major role in affecting battery cyclelife. The most important parameters in battery degradation are energy capacity and cyclelife. These parameters depend on temperature, depth of discharge (DOD), state of charge (SOC), charge and discharge rates (c-rate), battery application, type of battery, and battery manufacturer. However, battery degradation modeling becomes unrealized as the effects of these degradation factors cannot be analyzed and modeled individually. Therefore, the most important degradation factors are considered to be temperature, DOD, SOC, and c-rate. Several studies have shown that SOC can also be defined in the form of a DOD. A battery with DOD of d completes its charge-discharge cycle by discharging from 100% SOC to $(100 - d)$% SOC and then charging back to 100% SOC [34].

Li-ion battery manufacturers' datasheets show that the value of c-rate below 1 does not affect the energy capacity. However, when increasing the c-rate above 1, the energy capacity of a Li-ion battery starts decreasing [35,36]. The charge and discharge rate limits of a high energy capacity Li-ion battery storage system do not go beyond 0.5, which is discussed in [37], based on technical investigations. Therefore, the c-

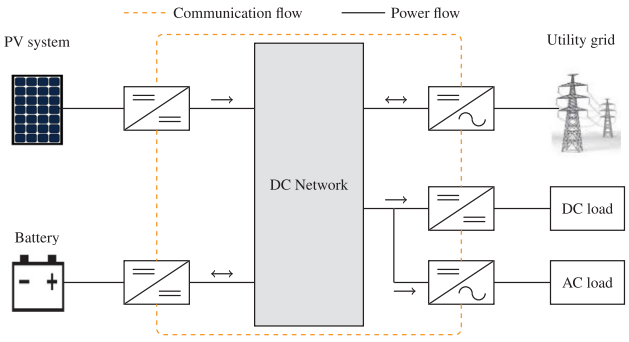

Fig. 1. DC MG architecture.

rate effect on battery degradation modeling is ignored. Moreover, effects of charge and discharges rate on battery cyclelife is negligible and it can be ignored too [38,39]. Hence, a BDC model is proposed considering the effects of temperature and DOD on its energy capacity and cyclelife.

2.1. Temperature

Temperature affects the chemical reaction rate of Li-ion battery, thus affecting its capacity. Arrhenius equation describes the increasing exponential dependence of reaction rate on temperature. Therefore, battery capacity increases with temperature due to increase in its chemical reaction rates. This increase in battery capacity means that the battery can provide more power at high temperatures. Arrhenius effect is expressed as [40]:

$$\Phi = \Phi_{ref}\left[\frac{E_a(\Phi)}{R}\left(\frac{1}{T_{ref}} - \frac{1}{T}\right)\right] \tag{1}$$

The regression model for temperature dependent battery energy capacity relation is determined using the data from Li-ion battery datasheet as shown in Fig. 2 [35]. The battery loses capacity to provide the same power at low temperatures due to metallic Lithium plating that causes electrolyte decomposition [41]. Eq. (2) describes the relation between battery capacity and temperature.

$$h_{\Xi}(T) = \alpha e^{-\beta T} + c \tag{2}$$

where $\alpha = -0.354$, $\beta = 0.0310$, and $c = 1.157$.

Li-ion battery usage at very high temperatures results in severely decreasing the cyclelife. This is caused by higher solid electrolyte interphase film accumulation, thus causing fast-er decay in cyclelife and increasing battery aging process [42,43]. The graphical relation between cyclelife and temperature provided in [34] and shown in Fig. 3, can be modeled as:

$$h_{\Upsilon}(T) = \begin{cases} \alpha_1 e^{-\beta_1 T} + \gamma_1, & -40\ ^\circ\text{C} \leqslant T < 0\ ^\circ\text{C} \\ \alpha_2 T + \beta_2, & 0\ ^\circ\text{C} \leqslant T < 18\ ^\circ\text{C} \\ \alpha_3 T + \beta_3, & 18\ ^\circ\text{C} \leqslant T < 50\ ^\circ\text{C} \\ \alpha_4 e^{-\beta_4 (T-50)} + \gamma_4, & 50\ ^\circ\text{C} \leqslant T \leqslant 80\ ^\circ\text{C} \end{cases} \tag{3}$$

where α_1, α_2, α_3, α_4, β_1, β_2, β_3, β_4, γ_1, γ_4 are the parameters of the aforementioned model that provide best fit to the experimental data. $\alpha_1 = -3050.056$, $\beta_1 = 0.023$, $\gamma_1 = 7811.54$, $\alpha_2 = 14.964$, $\beta_2 = 4767.474$ in this study. Similarly, $\alpha_3 = -6.99$, $\beta_3 = 5169.082$, $\alpha_4 = -149.889$, $\beta_4 = 0.117$, $\gamma_4 = 4981.68$.

2.2. Depth of discharge

Theoretically, DOD is defined as the absolute discharge relative to the related battery capacity. It is represented as SOC subtracted from 100% charge ($1 - SOC$). DOD has a minimal effect on battery power fading [44] and is ignored in power fading modeling. However, DOD causes mechanical stresses and side reactions in battery, which result in decreasing its cyclelife. Therefore, cyclelife is strongly dependent on DOD. The higher the DOD is, the lesser battery cyclelife will be. A relation between cyclelife and DOD of a Li-ion battery is obtained using practical results taken from [35], as presented in Fig. 4. Eq. (4) presents the logarithmic model that describes the effects of DOD on a battery cyclelife.

$$h_{\Upsilon}(d) = \alpha \log(d) + \beta \tag{4}$$

where d represents DOD of Li-ion battery. α and β are regression coefficients of cyclelife dependence on DOD. In this case, $\alpha = -5440.35$ and $\beta = 1191.54$.

2.3. Battery degradation cost

Several studies have proposed various battery degradation cost models incorporating mainly DOD and temperature effects. However, temperature effects are only considered in determining cyclelife or capacity fading of battery. In this paper, power fading due to temperature change is also performed by considering its effects on battery capacity. The effect of temperature on battery capacity is defined as the ratio of Ξ_T to Ξ_{ref}, as presented in (5).

$$\chi_T^{\Xi} = \frac{\Xi_T}{\Xi_{ref}} \tag{5}$$

Similarly, the effects of temperature and DOD on cyclelife are also defined as Υ_T to Υ_{ref} and Υ_d to Υ_{ref}, respectively. Eqs. (6) and (7) describe these two factors.

$$\chi_T^{\Upsilon} = \frac{\Upsilon_T}{\Upsilon_{ref}} \tag{6}$$

$$\chi_d^{\Upsilon} = \frac{\Upsilon_d}{\Upsilon_{ref}} \tag{7}$$

In respect of consideration of temperature and DOD, the BDC of a Li-ion battery, C^b, can be calculated using Eq. (8). A factor of $\frac{1}{2}$ is used to account for both charge and discharge actions during a cycle. The residual value (RV) is defined as economic value of the Li-ion battery at the end of its useful life. The proposed BDC model is developed based on engineering economic principles [45]. The BDC model computes present values of RV and annual operation and maintenance costs of the Li-ion battery with a discount rate dr and a lifetime of n years.

$$C^b = \frac{1}{2}\frac{[C_{inv}^b + \sum_{i=1}^{n} C_{om}^b (1+dr)^{-i}](1+dr)^n - RV}{(1+dr)^n \chi_T^{\Xi} \chi_T^{\Upsilon} \chi_d^{\Upsilon} \Upsilon_{ref} \Xi_{ref}} \tag{8}$$

3. PV system cost modeling

A need for distribution generation, energy supply to remote areas, and maturity in technology development pave the way for large deployment of PV systems worldwide. The overall global deployment status of PV systems is 385.6 GW until 2017, among which China, Japan, Germany, and USA are major contributors with the installation of 130.6 GW, 48.6 GW, 42.4 GW, and 41.1 GW of PV systems, respectively [46]. External factors, such as solar irradiance, temperature, and geographical location, affect the power generation output of PV systems. In this paper, the estimated power output of a PV system, with standard test conditions (STC) and nominal operating cell temperature (NOCT) conditions, is calculated as [47]:

$$P^{pv} = N^{pv} P_{STC}^{pv}\left[\frac{G}{G_{STC}}\{1 - \gamma(T_c - T_{STC})\}\right] \tag{9}$$

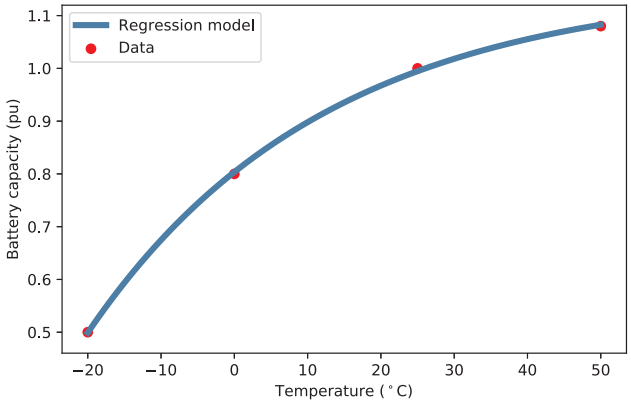

Fig. 2. Effect of temperature on Li-ion battery capacity.

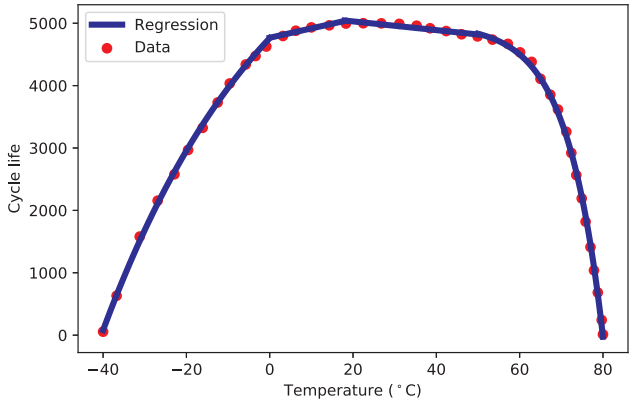

Fig. 3. Effect of temperature on Li-ion battery cyclelife at 50% DOD.

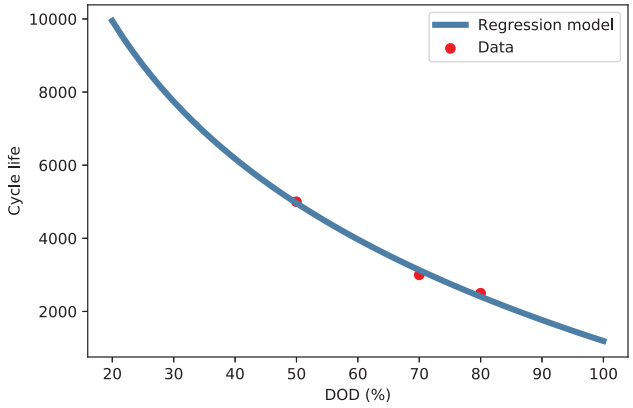

Fig. 4. Regression curve of Li-ion battery cyclelife vs DOD.

$$T_c = T + \frac{G}{G_{NOCT}}(NOCT - 20) \tag{10}$$

LCOE is a widely used metric to determine the electricity generation cost of various energy technologies over the system lifespan. Therefore, electricity production cost of a PV system is calculated based on LCOE. The investment cost of PV system includes capital cost of module and converters, labour installation cost, construction cost, land acquisition cost, and other hardware balance of system cost. Based on engineering economic principles, Eq. (11) can be used to calculate the PV system LCOE, C^{pv}, [48]. The energy output of the PV system is determined by averaging solar power over a time interval of one hour and summing it up all to get E_{an}^{pv}. The present values of C_{om}^{pv} and E_{an}^{pv} are computed each year with a dr over system life of n years. As PV system performance decreases with time, degradation factor, σ, is associated with E_{an}^{pv} after first year.

$$C^{pv} = \frac{C_{inv}^{pv} + \sum_{i=1}^{n} C_{om}^{pv}(1+dr)^{-i}}{\sum_{i=1}^{n} E_{an}^{pv}(1-\sigma)^{i-1}(1+dr)^{-i}} \tag{11}$$

The degradation in PV energy output is accounted to start from second year. Degradation occurs due to oxidation, thermal stresses, degradation of interconnections, weather effects, and microscopic cracks [49].

4. Incentive-based demand response modeling

DMO uses IDR in the proposed model as consumers give control access to DMO for shiftable load entities and receive incentives for it in return. Therefore, DMO can adjust the shiftable loads to off-peak periods, less generation supply periods, and scheduled islanding periods, while satisfying system constraints.

There are many types of shiftable loads that can be used in DR.

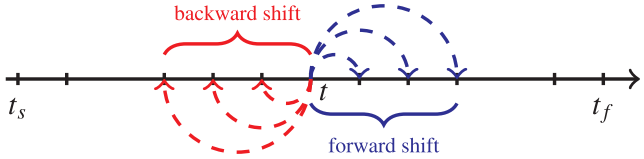

Fig. 5. DR mechanism.

Heating, ventilation, and air conditioning (HVAC), dishwasher, electric water heater, electric vehicle, and lightning are few examples. However, integration of these shiftable loads in the DC MG energy management model makes the problem non-convergent and requires higher computational time. Therefore, DMO aggregates shiftable load demand for each time t that helps in solving the developed model efficiently.

Consumers provide information to DMO about quantity and shiftable duration of their deferrable loads. These loads can be shifted backward, forward, or both. It is assumed that these informations are available to DMO. The process flow of DR mechanism with forward and backward shift time instants is shown in Fig. 5. The forward and backward shift instants can be consecutive or non-consecutive. They should remain between final time, t_f, and start time, t_s. Moreover, the cardinality of set of shiftable time instants, $\mathcal{T}_{sh}$, should be less than the total simulation time, as presented in (12). The cardinality refers to the size of a set.

$$|\mathcal{T}_{sh}| \leqslant t_f - t_s \tag{12}$$

DMO offers IDR to customers to participate in DR during normal and scheduled islanding periods. Scheduled islanding responsive IDR is introduced to encourage customers to shift load to normal operation period. It results in reducing lost load during scheduled islanding period. The IDR model is provided in (13).

$$\pi_t^{dr} = \begin{cases} (\delta_1 + \rho_1 z_t)\pi_t^{g+}, & t \in \mathcal{T}_1 \\ (\delta_2 + \rho_2 z_t)\pi_t^{g+}, & t \in \mathcal{T}_2 \quad \mathcal{T}_1 \cup \mathcal{T}_2 \cup \mathcal{T}_3 = \mathcal{T} \\ (\delta_3 + \rho_3 z_t)\pi_t^{g+}, & t \in \mathcal{T}_3 \end{cases} \tag{13}$$

IDR scaling factors are defined in range of $0 \leqslant \delta_1, \delta_2, \delta_3 < 1$ for off-peak, mid-peak, and on-peak periods, respectively. Similarly, scheduled islanding responsive IDR scaling parameters are also defined in the same range of $0 \leqslant \rho_1, \rho_2, \rho_3 < 1$. $\mathcal{T}_1$, $\mathcal{T}_2$, and $\mathcal{T}_3$ are sets of off-peak, mid-peak, and on-peak energy price time instants, respectively.

5. Energy management model

It is considered a grid-connected scalable DC MG consisting of a PV system, a Li-ion battery storage system, and shiftable and critical load demand. The proposed energy management model considers battery degradation model, DR, network power flow, and pre-determined islanding duration to optimize its optimal energy management operation while satisfying technical constraints. A centralized optimal operation is achieved by considering a central controller, DMO, that collects all the necessary information and optimizes the day-ahead energy management operation over a 24 h time horizon $\mathcal{T} := \{t_s, t_s + \Delta t, t_s + 2\Delta t, \ldots, t_f\}$. Detail of the energy management model are described in the following.

5.1. Objective function

The objective of DMO is to ensure the optimal operation of the microgrid by minimizing its operating cost. The objective function considers energy trading cost with UG, LCOE of a PV system, battery degradation cost, load shedding cost, and DR incentive cost. Eq. (14) presents the cost-function of DMO. As discussed in section II, BDC for each battery w and time t is described in (15). Selling energy price from DMO side is considered to be $\pi_t^{g-} = \lambda \pi_t^{g+}$, where λ should be $0 \leqslant \lambda < 1$.

It is assumed that buying, selling, and DR incentive prices are defined with order $\pi_t^{dr} < \pi_t^{g-} < \pi_t^{g+}$ for any $t \in \mathcal{T}$.

$$\min \sum_{t=t_s}^{t_f} \left\{ (\pi_t^{g+} P_t^{g+} - \pi_t^{g-} P_t^{g-}) + \sum_{v \in \mathcal{N}_\mathcal{V}} C^{pv} P_{v,t}^{pv} + \sum_{w \in \mathcal{N}_\mathcal{W}} C_{w,t}^{b} \left(\eta^{ch} P_{w,t}^{ch} + \frac{P_{w,t}^{dch}}{\eta^{dch}} \right) + \sum_{x \in \mathcal{N}_\mathcal{X}} (C^{voll} P_{x,t}^{ls} + \pi_t^{dr} P_{x,t}^{dr+}) \right\} \Delta t$$
$$\mathcal{N}_\mathcal{V} \subseteq \mathcal{N}, \mathcal{N}_\mathcal{W} \subseteq \mathcal{N}, \mathcal{N}_\mathcal{X} \subseteq \mathcal{N} \tag{14}$$

$$C_{w,t}^{b} = \frac{1}{2} \frac{[C_{inv}^{b} + \sum_{i=1}^{n} C_{om}^{b} (1+dr)^{-i}](1+dr)^{n} - RV}{(1+dr)^{n} \chi_{\Pi}^{\Xi} \chi_{\Pi}^{\Upsilon} \chi_{d}^{\Upsilon} \Upsilon_{w,ref} \Xi_{w,ref}}$$
$$w \in \mathcal{N}_\mathcal{W}, t \in \mathcal{T} \tag{15}$$

5.2. Grid connection constraints

The maximum power, transferred between UG and microgrid, is restricted by grid-tie line capacity. It is represented by P_{max}^{g} and provided in (16). For maintenance of grid-tie line, scheduled islanding status is denoted by z_t to present DC MG operation in islanded mode, as described in (17). The $\neg z_t$ is logical negation of z_t.

$$0 \leqslant P_t^{g+}, P_t^{g-} \leqslant P_{max}^{g}(\neg z_t) \qquad t \in \mathcal{T} \tag{16}$$

$$z_t = \begin{cases} 1, & \text{if islanding} \\ 0, & \text{otherwise} \end{cases} \quad t \in \mathcal{T} \tag{17}$$

5.3. PV system constraints

The PV system output power is discussed in section III. It is well known that the power output of PV systems varies with irradiance and temperature. Therefore, Eqs. (18) and (19) are modified to take into account the time t dependence of the generated power.

$$P_{v,t,av}^{pv} = N_v^{pv} P_{STC}^{pv} \left[\frac{G_t}{G_{STC}} (1 - \gamma (T_{c,t} - T_{STC}) \right]$$
$$v \in \mathcal{N}_\mathcal{V}, t \in \mathcal{T} \tag{18}$$

$$T_{c,t} = T_t + \frac{G_t}{G_{NOCT}} (NOCT - 20) \qquad t \in \mathcal{T} \tag{19}$$

Power output of the PV system for each bus v should remain within the limit of the maximum available PV power $P_{v,t,av}^{pv}$.

$$0 \leqslant P_{v,t}^{pv} \leqslant P_{v,t,av}^{pv} \qquad v \in \mathcal{N}_\mathcal{V}, t \in \mathcal{T} \tag{20}$$

5.4. Li-ion battery constraints

Charging and discharging power of the Li-ion battery is controlled by the charging and discharging rate variables. The relations between these variables are provided by Eqs. (21) and (22). These rates are restricted by the maximum limit defined in (23) and (24). Eq. (25) ensures that battery should either charge or discharge at any time $t \in \mathcal{T}$, but not both simultaneously. Eq. (26) defines intertemporal nature of battery, where its energy capacity changes with time t. In real time, DMO decides the final energy state of the battery according to the statistical analysis of the DC MG operation history. However, for this case study, it is assumed that initial and final state of energy capacity of the Li-ion battery should remain the same, as defined by (27). Eqs. (28) and (29) define maximum and minimum bounds on energy capacity of the Li-ion battery and the minimum energy capacity controlled by DOD at time t, respectively. Maximum energy capacity of the battery depends on temperature to consider power fading. However, temperature changes with time, thus changing maximum energy capacity of battery with time and making the proposed optimization problem intractable. Therefore, its average value, denoted by μ_T, is considered in calculating the maximum energy capacity in (30).

$$P_{w,t}^{ch} = R_{w,t}^{ch} \Xi_{w,ref} \qquad w \in \mathcal{N}_\mathcal{W}, t \in \mathcal{T} \tag{21}$$

$$P_{w,t}^{dch} = R_{w,t}^{dch} \Xi_{w,ref} \qquad w \in \mathcal{N}_\mathcal{W}, t \in \mathcal{T} \tag{22}$$

$$0 \leqslant R_{w,t}^{ch} \leqslant CR_{w,max} \qquad w \in \mathcal{N}_\mathcal{W}, t \in \mathcal{T} \tag{23}$$

$$0 \leqslant R_{w,t}^{dch} \leqslant DCR_{w,max} \qquad w \in \mathcal{N}_\mathcal{W}, t \in \mathcal{T} \tag{24}$$

$$R_{w,t}^{ch} R_{w,t}^{dch} = 0 \qquad w \in \mathcal{N}_\mathcal{W}, t \in \mathcal{T} \tag{25}$$

$$\Xi_{w,t} = \Xi_{w,t-1} + \left[\eta^{ch} P_{w,t}^{ch} - \frac{P_{w,t}^{dch}}{\eta^{dch}} \right] \Delta t \quad w \in \mathcal{N}_\mathcal{W}, t \in \mathcal{T} \tag{26}$$

$$\Xi_{w,t_f} = \Xi_{w,t_s} \qquad w \in \mathcal{N}_\mathcal{W} \tag{27}$$

$$\Xi_{w,min} \leqslant \Xi_{w,t} \leqslant \Xi_{w,max} \qquad w \in \mathcal{N}_\mathcal{W} \tag{28}$$

$$\Xi_{w,max} = \Xi_{ref} \chi_{\mu_T}^{\Xi} \qquad w \in \mathcal{N}_\mathcal{W} \tag{29}$$

$$\Xi_{w,min} = \Xi_{w,max}(1 - d) \qquad w \in \mathcal{N}_\mathcal{W} \tag{30}$$

5.5. DR constraints

Eqs. (31) and (32) define the shifted load from time t and recovered load at time t, respectively. Eq. (33) defines that DR load demand can be either shifted or recovered at time t, but both these processes cannot happen at the same time. Modified load demand after DR is presented in (34) and it cannot be more than the maximum value of the base load demand, which is controlled by (35). Eq. (36) assures that the total recovered DR load must be equal to the shifted DR load. Shifted DR load from time t to i and total shifted DR load from t are constrained by the maximum shiftable DR load, as established by (37). All the defined variables are non-negative, as presented in (38).

$$P_{x,t}^{dr+} = \sum_{\substack{i \in \mathcal{T}_{sh} \\ i \neq t}} P_{x,t,i}^{dr} \qquad x \in \mathcal{N}_\mathcal{X}, t \in \mathcal{T} \tag{31}$$

$$P_{x,t}^{dr-} = \sum_{\substack{i \in \mathcal{T}_{sh} \\ i \neq t}} P_{x,i,t}^{dr} \qquad x \in \mathcal{N}_\mathcal{X}, t \in \mathcal{T} \tag{32}$$

$$P_{x,t}^{dr+} P_{x,t}^{dr-} = 0 \qquad x \in \mathcal{N}_\mathcal{X}, t \in \mathcal{T} \tag{33}$$

$$P_{x,t}^{l} = L_{x,t}^{b} - P_{x,t}^{dr+} + P_{x,t}^{dr-} \qquad x \in \mathcal{N}_\mathcal{X}, t \in \mathcal{T} \tag{34}$$

$$\sum_{x \in \mathcal{N}_\mathcal{X}} P_{x,t}^{l} \leqslant \| \sum_{x \in \mathcal{N}_\mathcal{X}} L_{x,t}^{b} \|_\infty \qquad t \in \mathcal{T} \tag{35}$$

$$\sum_{t=t_s}^{t_f} \sum_{x \in \mathcal{N}_\mathcal{X}} P_{x,t}^{dr+} = \sum_{t=t_s}^{t_f} \sum_{x \in \mathcal{N}_\mathcal{X}} P_{x,t}^{dr-} \tag{36}$$

$$P_{x,t,i}^{dr}, P_{x,t}^{dr+} \leqslant P_{x,t,max}^{dr} \qquad x \in \mathcal{N}_\mathcal{X}, t \in \mathcal{T} \tag{37}$$

$$nb, nf, P_{x,t}^{dr+}, P_{x,t}^{dr-} \geqslant 0 \qquad x \in \mathcal{N}_\mathcal{X}, t \in \mathcal{T} \tag{38}$$

5.6. Network constraints

In a DC MG system, voltage of each bus should be considered and system losses have to be accounted while optimizing each generation source scheduling and DR. Otherwise, the proposed energy model cannot provide accurate results. Therefore, power flow constraints of the DC MG network are considered. Eq. (39) is the power injection equation for bus i. Bus voltages are constrained by lower and upper bounds, as presented in (40). Line losses and total system losses at time t are given in (41) and (42), respectively.

$$P_t^i = \sum_{\substack{j=1 \\ j\neq i}}^{\mathcal{N}} V_t^i (V_t^i - V_t^j) y_{ij} \qquad i \in \mathcal{N} \tag{39}$$

$$V_{min}^i \leqslant V_t^i \leqslant V_{max}^i \qquad i \in \mathcal{N} \tag{40}$$

$$P_{ij,t}^{loss} = (V_t^i - V_t^j)^2 y_{ij} \qquad j \neq i, (i,j) \in \mathcal{N}, t \in \mathcal{T} \tag{41}$$

$$P_t^{loss} = \sum_{i=1}^{\mathcal{N}-1} \sum_{j=i+1}^{\mathcal{N}} P_{ij,t}^{loss} \qquad t \in \mathcal{T} \tag{42}$$

5.7. Power balance constraint

Eq. (43) ensures that the generated total power must be equal to the total demand, lost load, and system losses of the DC MG at each time t. $P_{x,t}^l$ relation is already given in (34).

$$(P_t^{g+} - P_t^{g-}) + \sum_{v\in\mathcal{N}_\mathcal{V}} P_{v,t}^{pv} - \sum_{w\in\mathcal{N}_\mathcal{W}} (P_{w,t}^{ch} - P_{w,t}^{dch}) = \sum_{x\in\mathcal{N}_\mathcal{X}} (P_{x,t}^l - P_{x,t}^{ls}) + P_t^{loss} \qquad t \in \mathcal{T} \tag{43}$$

6. Numerical studies

Time of use (TOU) energy prices of buying electricity for summer and winter seasons are taken from the Ontario Energy Boa-rd [50]. The TOU rates are divided into three zones of off-peak, mid-peak, and on-peak hours. The TOU energy prices of selling electricity and DR incentive benefits are derived from TOU energy rates of buying electricity. The TOU energy prices of buying and selling electricity are shown in Fig. 6. DR incentive benefits are given in Table 1. Value of the lost load is assumed to be 2 $/kWh. A PV system of 15 kW is considered in this study. The rated capacity of the Li-ion battery is 38.4 kWh. Charging and discharging efficiency of Li-ion battery are taken to be 0.9. Residual value is assumed to be 30% of capital cost at the end of the battery life. It is assumed that the battery is 70% charged before starting operation. Value of investment cost of the PV system for DC applications is taken from [51]. Capital cost of the Li-ion battery is obtained from [52]. Operation and maintenance costs of the PV system and the Li-ion battery are considered 22 $/kW-year and 20 $/kW-year, respectively. Degradation factor of the PV system is assumed to be 0.05% and the discount rate is considered as 5%. The hourly temperature profiles of Dammam and Brest regions, in July and December months, are shown in Fig. 7 [53] for 24 h operation. These months are considered to take into account the effects of temperature on performance of the PV system and the Li-ion battery for summer and winter seasons, respectively. Fig. 7 shows the modified hourly load profiles of 24 h of Dammam and Brest regions during July and December [54,55]. The hourly irradiances of these regions are taken from [56] for a period of 24 h. Fig. 7 also shows the power output of 15 kW_p PV system. These load profiles and PV system are considered for a 6-bus system, shown in Fig. 8. The line data and base voltage of this 6-bus system are taken from [57]. The power demand at load buses 4, 5, and 6 are assumed to be 25%, 45%, and 30% of total load, respectively. The minimum and maximum limit on each bus voltage is 0.95 pu and 1.05 pu, respectively. The proposed nonlinear programming model is solved by the primal-dual interior point method with GEKKO package in Python [58,59].

6.1. PV system cost and energy output

Hot and cold weather climate regions are selected to assess the power output and LCOE of the PV system. Dammam, Saudi Arabia is considered for hot weather climate, while Brest, France is chosen for cold weather climate region. Temperature and irradiance data of these cities are taken from [53,56]. The comparison of the PV system LCOE for these cities is carried out. LCOE and annual energy output of Dammam and Brest regions are shown in Fig. 9. The LCOE of PV system at Dammam and Brest regions are 0.067 $/kWh and 0.1 $/kWh, respectively. The main reason of a higher LCOE for the later region is low irradiance. The annual energy output of first year of the PV system at Dammam and Brest regions is calculated to be 33.01 MWh and 22.05 MWh, respectively.

6.2. Impact of temperature

The ideal operating temperature range, 10 °C to 50 °C, for a Li-ion battery operation is discussed in [60]. It shows that decreasing this temperature range leads to wasteful thermal management of the battery and increasing it leads to fast rise in the aging process. Temperature strongly affects discharged capacity of BDC of the Li-ion battery. Fig. 10 shows the change in the BDC with DOD and temperature. BDC strongly increases with the decrease in temperature below 10 °C and increase in DOD. BDC cost analysis shows that a DOD of 0.6 and a temperature above 10 °C provide lower cost for Li-ion battery operation.

As temperature depends on geographical locations, the BDC is therefore location-dependent. Therefore, two hot and cold climate regions are considered to study the Li-ion battery degradation. The discharged capacity and variation in BDC of the Li-ion battery during a 24 h period in December is shown in Fig. 11. The discharged capacity of battery at Dammam is higher than Brest due to temperature differences of these regions. At Brest, low temperature causes reduction in available discharge capacity, thus rising the BDC cost. Moreover, the BDC variation at Brest is higher than Dammam.

The operating cost of the DC MG is also analyzed considering temperature dependence of the Li-ion battery degradation cost. For this purpose, a grid-connected DC MG without PV is considered for both Dammam and Brest winter cases. The same values of load demand are taken for this study. Results presented in Table 2 show an increase in the operating cost of the DC MG at Brest site due to lesser availability of discharge capacity and higher BDC. Hence, operating cost of the DC MG increases by 1.1% for 24 h operation at Brest. These results show that the temperature considerably increases the operating cost of a DC MG system in cold weather regions. Therefore, a temperature-dependent BDC model of a Li-ion battery is more practical in deciding daily optimal scheduling of a DC MG system.

6.3. Brest and Dammam during summer

In this case, the DC MG operation is studied for the cases of no DR, DR, and short period scheduled islanding in Brest and Dammam for 24 h in July. Figs. 12 and 13 show line losses, voltage profiles of buses, and optimal power scheduling for Brest and Dammam, respectively for 24 h operation without DR. The system losses remain very low, below

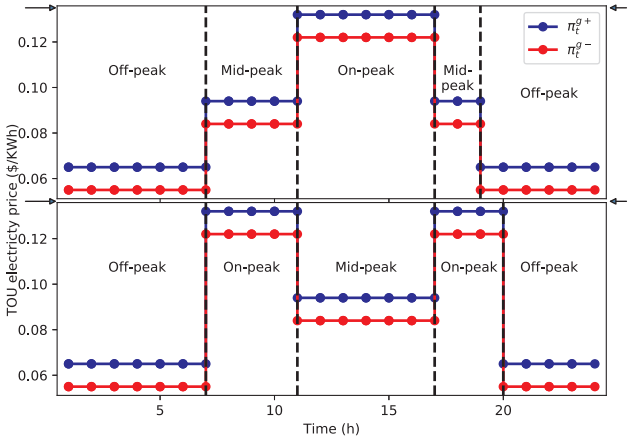

Fig. 6. TOU energy rates for summer (top) and winter (bottom).

Table 1
Time-of-use DR incentive.

	Off-peak	Mid-peak	On-peak
DR incentive (grid connected) [$/MWh]	0	5	10
DR incentive (scheduled islanding) [$/MWh]	10	10	10

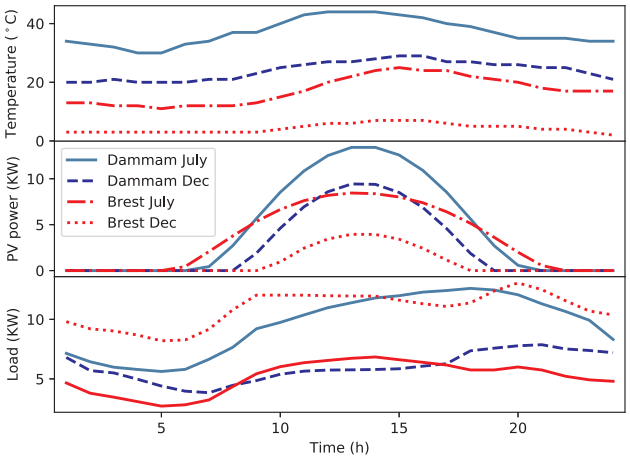

Fig. 7. Temperature profiles of Dammam and Brest regions (top), Power generation output of 15 kW_p PV system for Dammam and Brest regions during December and July (mid), Load profiles of Dammam and Brest regions (bottom).

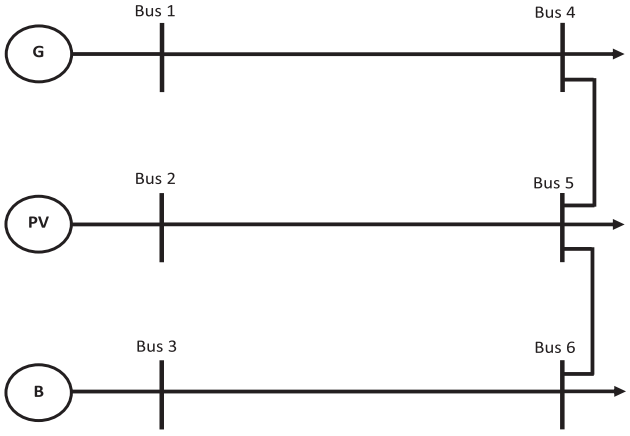

Fig. 8. Single line diagram of 6-bus system.

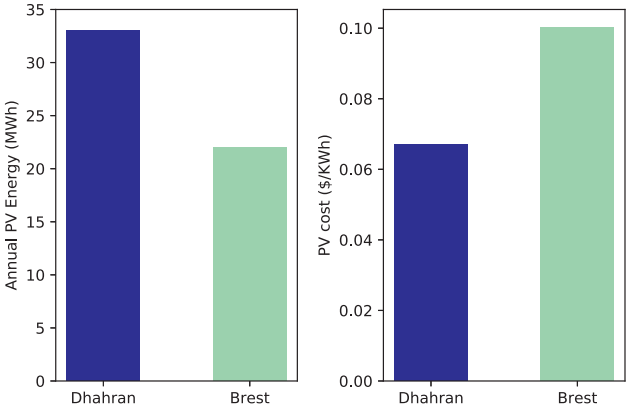

Fig. 9. Annual energy output (left) and LCOE (right) of PV system.

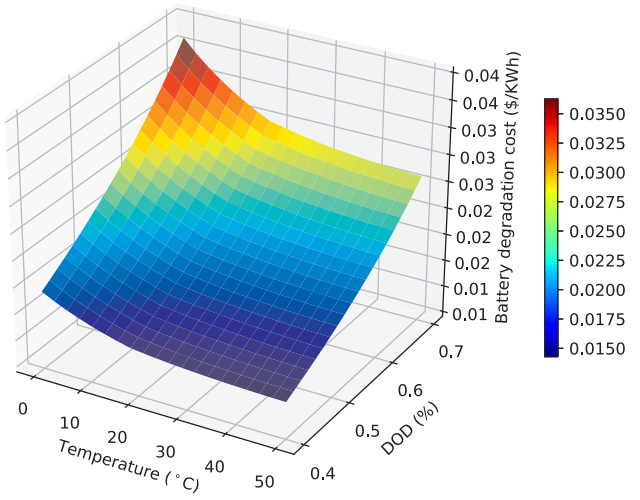

Fig. 10. Effects of temperature and DOD on Li-ion battery degradation cost.

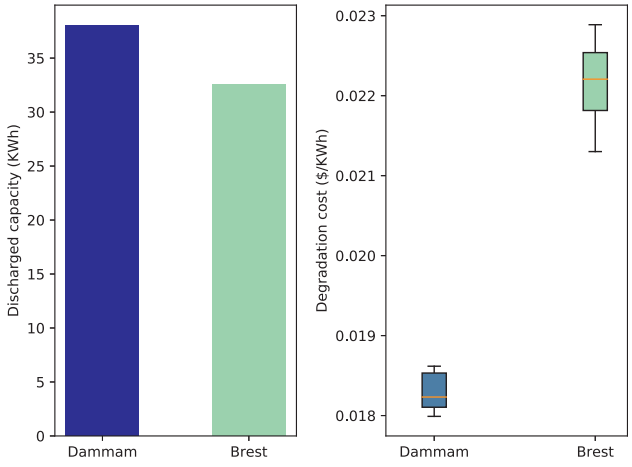

Fig. 11. Maximum available discharged capacity (left) and degradation cost variation (right) of Li-ion battery during 24 h in December.

Table 2
Impact of temperature on operating cost of DC MG without PV.

	Trading cost (pu)	Battery cost (pu)	Total cost (pu)
Dammam	0.947	0.053	1.0
Brest	0.957	0.054	1.011
Cost increase at Brest	0.01	0.001	0.011 (1.1%)

0.08 kW during 24 h period. Simulation results for Brest and Dammam with DR of 6 h shift, line losses, voltage profiles of buses, load before and after DR, and dispatch for energy balance of the DC MG are given by Figs. 14 and 15, respectively. The 6 h DR shift consists of 3 h consecutive forward shift and 3 h consecutive backward shift. The maximum shiftable load is assumed to be 10% of the total load at bus x and time t. These figures show that the load demand shifts from high energy price period, thus reducing the operating cost of the DC MG with the introduction of DR. In this study, the shiftable power consumption can be either increased or decreased at time instant t and 3 h consecutive forward and backward shift duration are considered. Therefore, load at t = 14 h will not shift as load is being decreased at three time instants before and after it. Moreover, shiftable load moves to mid-peak periods due to the allowed 3 h forward and backward shifts. However, in case of all-day shift, shiftable load shifts from on-peak energy price periods to off-peak energy periods, thus achieving the minimum DC MG operation

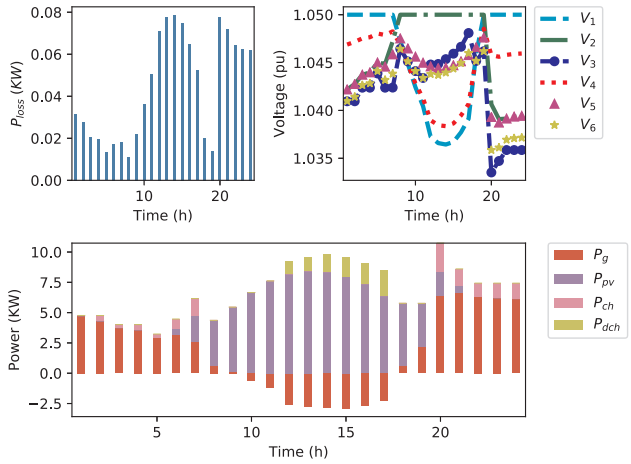

Fig. 12. Power losses (top left), bus voltages (top right), and scheduling (bottom) of DC MG without DR at Brest in summer.

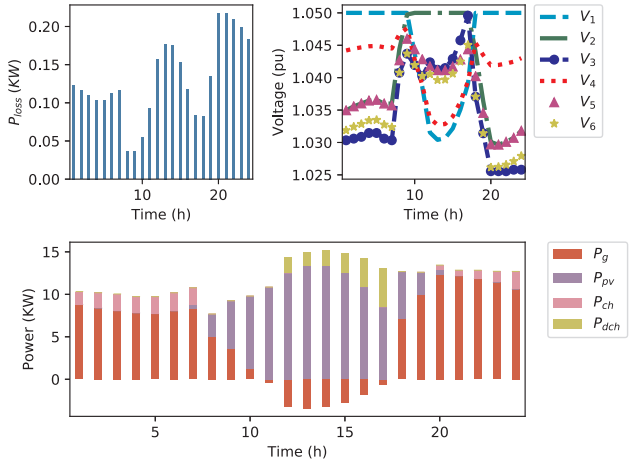

Fig. 13. Power losses (top left), bus voltages (top right), and scheduling (bottom) of DC MG without DR at Dammam in summer.

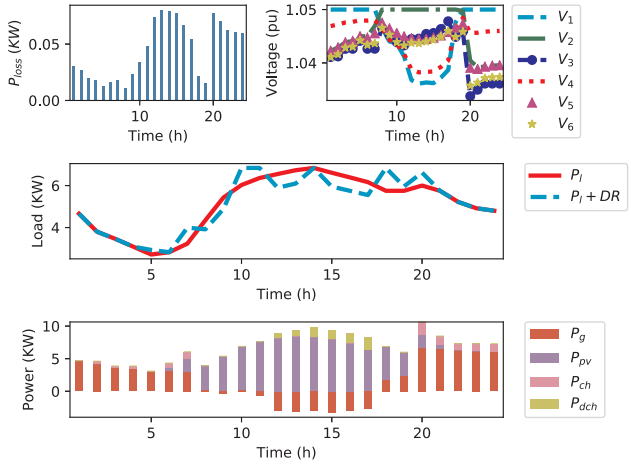

Fig. 14. Power losses (top left), bus voltages (top right), load with DR (mid), and dispatch (bottom) for DC MG with DR at Brest in summer.

cost. However, the DC MG cost reduces with increasing DR shift duration, which is shown in Table 3. For 10% of shiftable load, the DC MG cost reduces from 0.99 pu (1%) for 6 h shift duration to 0.944 pu (5.6%) for all-day shift. For shiftable load equal to 20% of total load, the DC MG cost reduces from 0.985 pu (1.5%) for 6 h shift to 0.912 pu

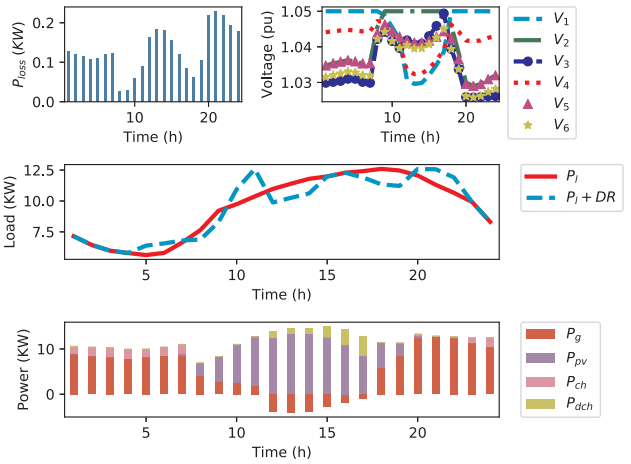

Fig. 15. Power losses (top left), bus voltages (top right), load with DR (mid), and dispatch (bottom) for DC MG with DR at Dammam in summer.

(8.8%) for 10 h shift. If shiftable load availability is 30% of total load, the DC MG cost reduces from 0.983 pu (1.7%) for 6 h shift to 0.881 pu (11.9%) for all-day shift. No load shedding happens for normal operating conditions. Hence, the DMO should have a contract with consumers of all-day shift to achieve cost-effective DC MG operation and consumers will therefore receive incentives in return.

Considering scheduled maintenance of grid tie-line connection, islanding may happen for short interval of time during a 24 h period. This case is also studied. Figs. 16 and 17 show line losses, voltage profiles of buses, load before and after 6 h shift DR, and dispatch for energy balance of the DC MG during islanding for Brest and Dammam, respectively. The Li-ion battery discharges during high price period and charges back to the maximum threshold to provide energy during the islanding period. Before islanding, battery charges at high rate and voltage of battery bus steeply decreases to around 1.03 pu, which results in higher system losses. Scheduled islanding is shown during the PV power absence periods. If islanding happens during excess PV power periods, the PV system will supply power to load buses, thus no load shedding will happen.

The operating cost comparison of the DC MG for different DR levels and DR duration periods for Brest is presented in Table 4. This table presents the cost comparison considering an islanding period of 3 h. As the islanding period is considered for 3 h only, operating cost of the DC MG remains the same with respect to the demand shift period of 6 h onwards, but it strongly decreases with the increase in DR shift value.

Table 5 provides the cost comparison of the DC MG for different DR values and DR shifting hours for Dammam region. For 6 h shift, operating cost of the DC MG decreases by 1.1%, 1.6%, 1.9% for DR of 10%, 20%, and 30% of the base load, respectively. However, it noticeably decreases with the increase in DR time shift for the same values of the shifted load. Similarly, Table 6 presents the cost comparison considering an islanding period of 3 h. This table shows that the operating cost decreases with the increase in the value of the shifted load.

Table 3
Operating cost of DC MG without islanding for Brest in summer.

DR limit	DR duration			
	No DR (pu)	6 h (pu)	10 h (pu)	23 h (pu)
10% of $\sum_{x\in N_X} L^b_{x,t}$	1.0	0.990	0.957	0.944
20% of $\sum_{x\in N_X} L^b_{x,t}$	1.0	0.985	0.942	0.912
30% of $\sum_{x\in N_X} L^b_{x,t}$	1.0	0.983	0.932	0.881

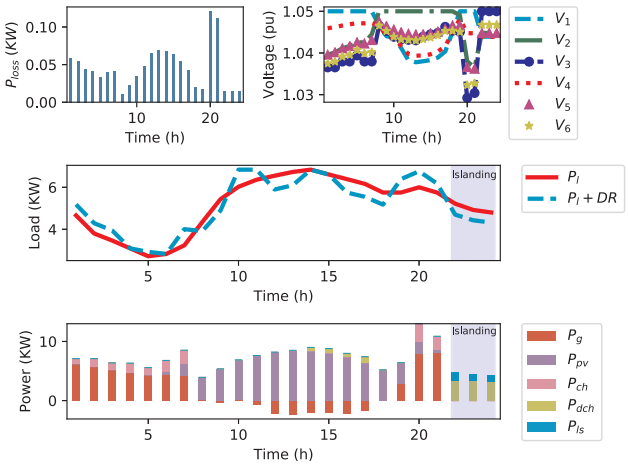

Fig. 16. Power losses (top left), bus voltages (top right), load with DR (mid), and dispatch (bottom) for DC MG with DR and islanding at Brest in summer.

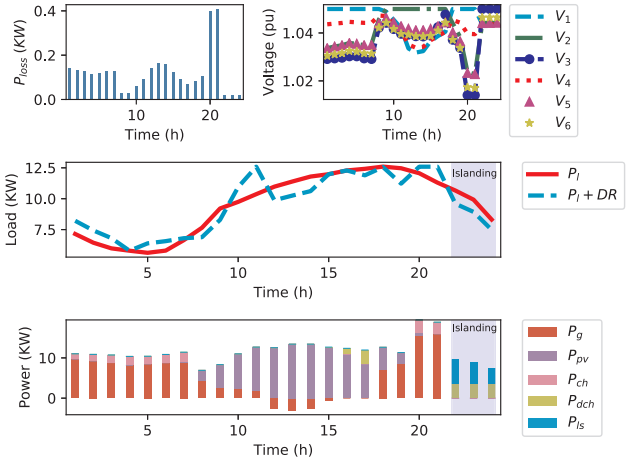

Fig. 17. Power losses (top left), bus voltages (top right), load with DR (mid), and dispatch (bottom) for DC MG with DR and islanding at Dammam in summer.

Table 4
Operating cost of DC MG with islanding for Brest in summer.

DR limit	DR duration			
	No DR (pu)	6 h (pu)	10 h (pu)	23 h (pu)
10% of $\sum_{x\in N_X} L^b_{x,t}$	1.0	0.858	0.845	0.838
20% of $\sum_{x\in N_X} L^b_{x,t}$	1.0	0.720	0.704	0.685
30% of $\sum_{x\in N_X} L^b_{x,t}$	1.0	0.584	0.564	0.533

Table 5
Operating cost of DC MG without islanding for Dammam in summer.

DR limit	DR duration			
	No DR (pu)	6 h (pu)	10 h (pu)	23 h (pu)
10% of $\sum_{x\in N_X} L^b_{x,t}$	1.0	0.989	0.964	0.950
20% of $\sum_{x\in N_X} L^b_{x,t}$	1.0	0.984	0.951	0.911
30% of $\sum_{x\in N_X} L^b_{x,t}$	1.0	0.981	0.941	0.873

Table 6
Operating cost of DC MG with islanding for Dammam in summer.

DR limit	DR duration			
	No DR (pu)	6 h (pu)	10 h (pu)	23 h (pu)
10% of $\sum_{x\in N_X} L^b_{x,t}$	1.0	0.889	0.885	0.877
20% of $\sum_{x\in N_X} L^b_{x,t}$	1.0	0.780	0.774	0.757
30% of $\sum_{x\in N_X} L^b_{x,t}$	1.0	0.671	0.663	0.657

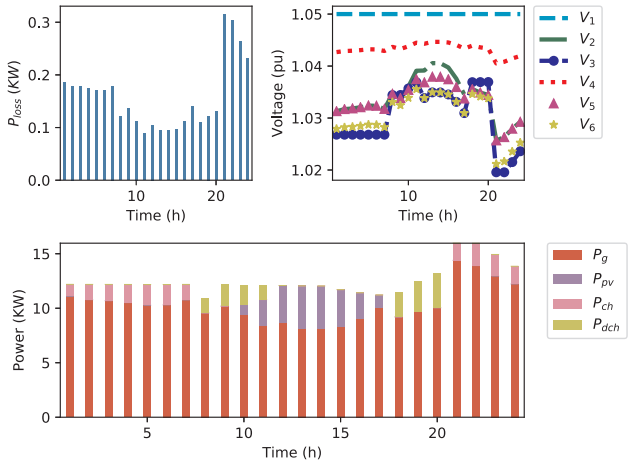

Fig. 18. Power losses (top left), bus voltages (top right), and scheduling (bottom) of DC MG without DR at Brest in winter.

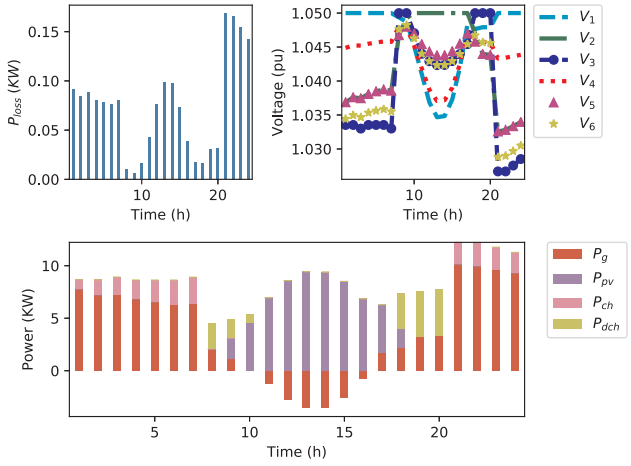

Fig. 19. Power losses (top left), bus voltages (top right), and scheduling (bottom) of DC MG without DR at Dammam in winter.

6.4. Brest and Dammam during winter

In this case, the DC MG operation at Brest and Dammam in December is studied for the cases of no DR, DR, and short period scheduled islanding of 3 h. Figs. 18 and 19 show line losses, voltage profiles of buses, and optimal power scheduling at Brest and Dammam, respectively, for 24 h operation without DR. At Brest, due to battery charging and high load demand, load and battery bus voltages decreases sharply and produces maximum line losses of 0.31 kW. Optimization results with DR of 6 h shift are given by Figs. 20 and 21 for Brest and Dammam regions, respectively. DR load is shifted to mid-peak price periods as 3 h forward and backward shifts are considered. However, with the increase in DR shift duration, the shiftable load moves to off-peak price periods, thus reducing the DC MG operation

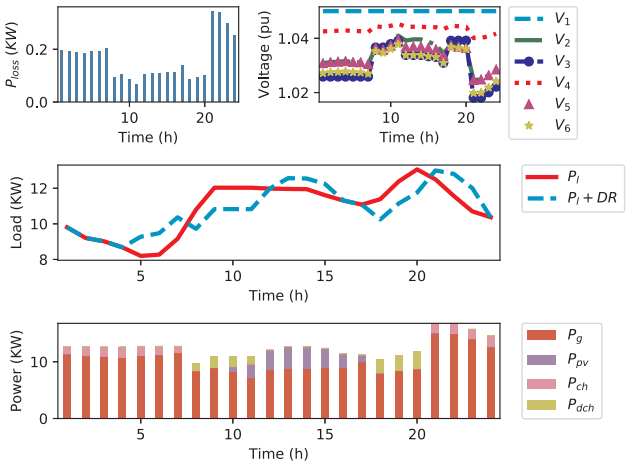

Fig. 20. Power losses (top left), bus voltages (top right), load with DR (mid), and dispatch (bottom) for DC MG with DR at Brest in winter.

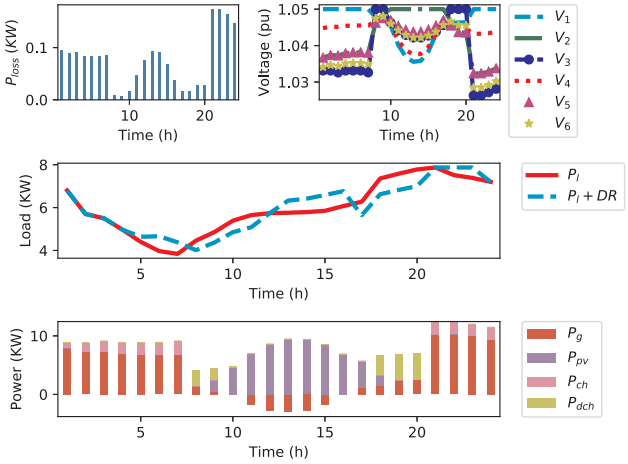

Fig. 21. Power losses (top left), bus voltages (top right), load with DR (mid), and dispatch (bottom) for DC MG with DR at Dammam in winter.

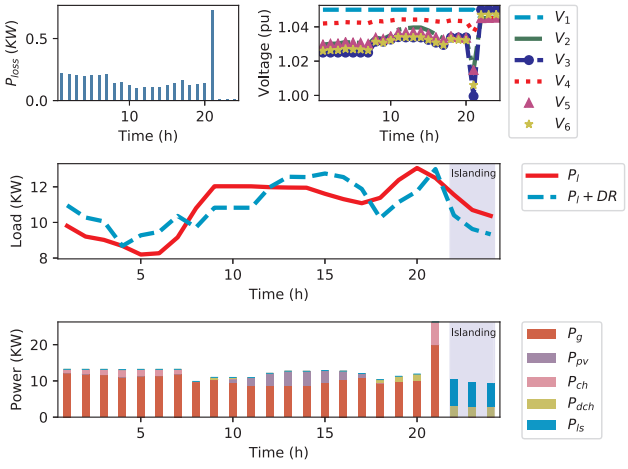

Fig. 22. Power losses (top left), bus voltages (top right), load with DR (mid), and dispatch (bottom) for DC MG with DR and islanding at Brest in winter.

cost effectively. There is no load shedding in normal operation.

Figs. 22 and 23 show line losses, voltage profiles of buses, and optimal power scheduling at Brest and Dammam, respectively, for 24 h operation in December for a 3 h scheduled islanding period with a DR of 6 h shift. These figures show that the battery charges at a high *c*-rate

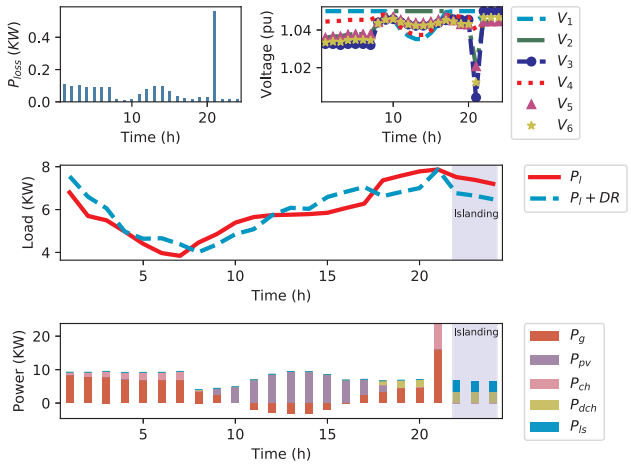

Fig. 23. Power losses (top left), bus voltages (top right), load with DR (mid), and dispatch (bottom) for DC MG with DR and islanding at Dammam in winter.

Table 7
Operating cost of DC MG without islanding for Brest in winter.

DR limit	DR duration			
	No DR (pu)	6 h (pu)	10 h (pu)	23 h (pu)
10% of $\sum_{x\in N_X} L^b_{x,t}$	1.0	0.982	0.978	0.969
20% of $\sum_{x\in N_X} L^b_{x,t}$	1.0	0.968	0.957	0.938
30% of $\sum_{x\in N_X} L^b_{x,t}$	1.0	0.957	0.940	0.920

Table 8
Operating cost of DC MG with islanding for Brest in winter.

DR limit	DR duration			
	No DR (pu)	6 h (pu)	10 h (pu)	23 h (pu)
10% of $\sum_{x\in N_X} L^b_{x,t}$	1.0	0.907	0.906	0.901
20% of $\sum_{x\in N_X} L^b_{x,t}$	1.0	0.816	0.815	0.806
30% of $\sum_{x\in N_X} L^b_{x,t}$	1.0	0.725	0.719	0.715

Table 9
Operating cost of DC MG without islanding for Dammam in winter.

DR limit	DR duration			
	No DR (pu)	6 h (pu)	10 h (pu)	23 h (pu)
10% of $\sum_{x\in N_X} L^b_{x,t}$	1.0	0.982	0.964	0.952
20% of $\sum_{x\in N_X} L^b_{x,t}$	1.0	0.967	0.946	0.918
30% of $\sum_{x\in N_X} L^b_{x,t}$	1.0	0.953	0.929	0.890

Table 10
Operating cost of DC MG with islanding for Dammam in winter.

DR limit	DR duration			
	No DR (pu)	6 h (pu)	10 h (pu)	23 h (pu)
10% of $\sum_{x\in N_X} L^b_{x,t}$	1.0	0.872	0.867	0.862
20% of $\sum_{x\in N_X} L^b_{x,t}$	1.0	0.752	0.738	0.728
30% of $\sum_{x\in N_X} L^b_{x,t}$	1.0	0.671	0.61	0.602

just one hour before islanding. At this time, the battery bus voltage decreases sharply to just below 1.0 pu and increases line losses.

The operating cost comparison of the DC MG at Brest for different DR levels and DR duration periods is presented in Table 7. This table shows that operating cost of the DC MG is decreasing with the increase of the demand shift period and the DR shift limit. For 6 h DR shift, on-peak instants load can be shifted to mid-peak price periods only, thus reducing cost by only 1.8%, 2.2%, and 3.1% for a shiftable load of 10%, 20%, and 30% of the total load, respectively. However, the shiftable load moves to off-peak price periods in all-day shift duration, thus resulting in higher cost reduction of 4.3%, 6.0%, and 8.0% for a shiftable load of 10%, 20%, and 30% of the total load, respectively. Similarly, Table 8 presents the cost comparison considering an islanding period of 3 h. As the islanding period is considered for 3 h only, therefore operating cost of the DC MG remains the same with respect to the demand shift period of 6 h onwards, but it remarkably decreases with the increase in DR shifting values with respect to the base load.

Table 9 refers to operating cost of the DC MG at Dammam for different DR values and DR shift periods in terms of base load. This table clearly shows that the operating cost of the DC MG is decreasing with the increase of the demand shift and the DR shift limit. Similarly, Table 10 presents the cost comparison considering an islanding period of 3 h. Operating cost considerably decreases for 6 h shift period by 32.9% for 30% shiftable demand of the base load. It cannot decrease more due to the maximum limit on recovered demand that can be shifted at any time *t*. However, it decreases by 39% and 39.8% for 10 h and 23 h period for the same amount of shiftable demand.

6.5. Real world applications

In energy management operation of the DC MG, decision strategies and informations are exchanged between local controllers and the DC MG operator using communication links. In DC MGs, such as rural, residential, and remote areas microgrids, communication technologies are decided on the basis of data rate and infrastructure cost. ZigBee, Wi-Fi, and Z-Wave are more suitable options. Low cost embedded systems, like Arduino, STM32, Rasberry Pi, and BeagleBone, can be adopted by local controllers to collect information and perform neccessay control actions. The DC MG operator is a human-to-machine system that performs energy management operation with the help of local controllers and a SCADA platform. The developed energy management model makes decision strategies with the information from all external factors and energy sources. It can be integrated in microgrid energy management modules, which are currently being developed by many energy companies as Schneider Electric, ABB, EDF, ENGIE, Alstom, Siemens, Tesla, and so forth, for optimal and efficient operation of microgrids. Hence, the developed model can be used for economic operation of a DC MG in the future.

7. Conclusion

In this paper, an optimization model was developed to minimize the operating cost of a DC microgrid. The proposed model includes aging factors-dependent practical degradation cost model of a Li-ion battery using real data. This model can be generalized to other types of batteries as they depict almost the same behavior. The optimization model also includes islanding-dependent demand response incentive to encourage active participation of customers during scheduled maintenance of grid-tie line. Levelized cost of photovoltaic system was also calculated using real data to obtain accurate cost for hot and cold climate regions. System losses and nodal voltages were also studied, as they are imperative in achieving realistic and efficient operation of a DC microgrid. Results analysis proves that, introducing islanding responsive demand response incentive and increasing the value of the shifted load demand and the demand response shift duration, greatly reduces the operating cost of the DC microgrid. Finally, temperature effects on operating cost of the DC microgrid without a photovoltaic system were analyzed. They show higher cost for cold climate region due to increased power fading of a Li-ion battery at low temperature. The obtained results confirmed that the integration of battery degradation cost and islanding responsive demand response incentives in DC microgrid applications would significantly influence the operating cost.

References

[1] Zia MF, Elbouchikhi E, Benbouzid M. Microgrids energy management systems: a critical review on methods, solutions, and prospects. Appl Energy 2018;222:1033–55.
[2] Stadler M, Cardoso G, Mashayekh S, Forget T, DeForest N, Agarwal A, et al. Value streams in microgrids: a literature review. Appl Energy 2016;162:980–9.
[3] Kumar D, Zare F, Ghosh A, et al. Dc microgrid technology: system architectures, ac grid interfaces, grounding schemes, power quality, communication networks, applications and standardizations aspects. IEEE Access 2017;5:12230–56.
[4] Wang C, Yan J, Marnay C, Djilali N, Dahlquist E, Wu J, et al. Distributed energy and microgrids (DEM). Appl Energy 2018;210:685–9.
[5] Bullich-Massagué E, Díaz-González F, Aragüés-Peñalba M, Girbau-Llistuella F, Olivella-Rosell P, Sumper A. Microgrid clustering architectures. Appl Energy 2018;212:340–61.
[6] Wu P, Huang W, Tai N, Liang S. A novel design of architecture and control for multiple microgrids with hybrid AC/DC connection. Appl Energy 2018;210:1002–16.
[7] Boroyevich D, Cvetković I, Dong D, Burgos R, Wang F, Lee F. Future electronic power distribution systems a contemplative view. 12th International Conference on Optimization of Electrical and Electronic Equipment (OPTIM). IEEE; 2010. p. 1369–80.
[8] Herrera L, Zhang W, Wang J. Stability analysis and controller design of dc microgrids with constant power loads. IEEE Trans Smart Grid 2017;8(2):881–8.
[9] Dragičević T, Lu X, Vasquez JC, Guerrero JM. Dc microgrids–part i: a review of control strategies and stabilization techniques. IEEE Trans Power Electron 2016;31(7):4876–91.
[10] Aneke M, Wang M. Energy storage technologies and real life applications—a state of the art review. Appl Energy 2016;179:350–77.
[11] Sanjeev P, Padhy NP, Agarwal P. Peak energy management using renewable integrated dc microgrid. IEEE Trans Smart Grid 2018;9(5):4906–17.
[12] Chaudhari K, Ukil A, Kumar KN, Manandhar U, Kollimalla SK. Hybrid optimization for economic deployment of ess in pv-integrated ev charging stations. IEEE Trans Ind Inf 2018;14(1):106–16.
[13] Badawy MO, Sozer Y. Power flow management of a grid tied pv-battery system for electric vehicles charging. IEEE Trans Ind Appl 2017;53(2):1347–57.
[14] Chalise S, Sternhagen J, Hansen TM, Tonkoski R. Energy management of remote microgrids considering battery lifetime. Electric J 2016;29(6):1–10.
[15] Bordin C, Anuta HO, Crossland A, Gutierrez IL, Dent CJ, Vigo D. A linear programming approach for battery degradation analysis and optimization in offgrid power systems with solar energy integration. Renew Energy 2017;101:417–30.
[16] Su W, Wang J, Roh J. Stochastic energy scheduling in microgrids with intermittent renewable energy resources. IEEE Trans Smart Grid 2014;5(4):1876–83.
[17] Zhang Y, Lundblad A, Campana PE, Benavente F, Yan J. Battery sizing and rule-based operation of grid-connected photovoltaic-battery system: a case study in Sweden. Energy Convers Manage 2017;133:249–63.
[18] Cai J, Zhang H, Jin X. Aging-aware predictive control of PV-battery assets in buildings. Appl Energy 2019;236:478–88.
[19] Cardoso G, Brouhard T, DeForest N, Wang D, Heleno M, Kotzur L. Battery aging in multi-energy microgrid design using mixed integer linear programming. Appl Energy 2018;231:1059–69.
[20] Nguyen TA, Crow ML. Stochastic optimization of renewable-based microgrid operation incorporating battery operating cost. IEEE Trans Power Syst 2016;31(3):2289–96.
[21] Cicconi P, Landi D, Germani M. Thermal analysis and simulation of a li-ion battery pack for a lightweight commercial EV. Appl Energy 2017;192:159–77.
[22] Spector J. Lithium-ion storage installs could grow 55% every year through 2022. Tech. rep. Massachusetts, United States: Greentech Media; 2018.
[23] Jin M, Feng W, Liu P, Marnay C, Spanos C. MOD-DR: microgrid optimal dispatch with demand response. Appl Energy 2017;187:758–76.
[24] Gu C, Yan X, Yan Z, Li F. Dynamic pricing for responsive demand to increase distribution network efficiency. Appl Energy 2017;205:236–43.
[25] Yu D, liu H, Bresser C. Peak load management based on hybrid power generation and demand response. Energy 2018;163:969–85.
[26] Anjo J, Neves D, Silva C, Shivakumar A, Howells M. Modeling the long-term impact of demand response in energy planning: the portuguese electric system case study. Energy 2018;165:456–68.
[27] Mohsenzadeh A, Pang C, Haghifam M-R. Determining optimal forming of flexible microgrids in the presence of demand response in smart distribution systems. IEEE Syst J 2018;12(4):3315–23.
[28] Wang J, Zhong H, Ma Z, Xia Q, Kang C. Review and prospect of integrated demand response in the multi-energy system. Appl Energy 2017;202:772–82.
[29] Siano P. Demand response and smart grids – a survey. Renew Sustain Energy Rev 2014;30:461–78.
[30] Gong Y, Cai Y, Guo Y, Fang Y. A privacy-preserving scheme for incentive-based

demand response in the smart grid. IEEE Trans Smart Grid 2016;7(3):1304–13.
[31] Zhou Z, Benbouzid M, Charpentier JF, Scuiller F, Tang T. A review of energy storage technologies for marine current energy systems. Renew Sustain Energy Rev 2013;18:390–400.
[32] Stiaszny B, Ziegler JC, Krauß EE, Zhang M, Schmidt JP, Ivers-Tiffée E. Electrochemical characterization and post-mortem analysis of aged limn2o4–nmc/graphite lithium ion batteries part ii: calendar aging. J Power Sources 2014;258:61–75.
[33] Sarasketa-Zabala E, Martinez-Laserna E, Berecibar M, Gandiaga I, Rodriguez-Martinez L, Villarreal I. Realistic lifetime prediction approach for li-ion batteries. Appl Energy 2016;162:839–52.
[34] Zhou C, Qian K, Allan M, Zhou W. Modeling of the cost of ev battery wear due to v2g application in power systems. IEEE Trans Energy Convers 2011;26(4):1041–50.
[35] Lithium—Smart $LiFePO_4$, Victron Energy, JG Almere Haven, Netherland.
[36] ION Power Battery Pack—40290203, Whisper Power, JB Drachten, Netherland.
[37] Zeh A, Müller M, Naumann M, Hesse HC, Jossen A, Witzmann R. Fundamentals of using battery energy storage systems to provide primary control reserves in Germany. Batteries 2016;2(3):29.
[38] Lam L, Bauer P. Practical capacity fading model for li-ion battery cells in electric vehicles. IEEE Trans Power Electron 2013;28(12):5910–8.
[39] Cordoba-Arenas A, Onori S, Guezennec Y, Rizzoni G. Capacity and power fade cycle-life model for plug-in hybrid electric vehicle lithium-ion battery cells containing blended spinel and layered-oxide positive electrodes. J Power Sources 2015;278:473–83.
[40] Sarre G, Blanchard P, Broussely M. Aging of lithium-ion batteries. J Power Sources 2004;127(1-2):65–71.
[41] Vetter J, Novák P, Wagner MR, Veit C, Möller K-C, Besenhard J, et al. Ageing mechanisms in lithium-ion batteries. J Power Sources 2005;147(1-2):269–81.
[42] Agubra V, Fergus J. Lithium ion battery anode aging mechanisms. Materials 2013;6(4):1310–25.
[43] Bloom I, Cole B, Sohn J, Jones S, Polzin E, Battaglia V, et al. An accelerated calendar and cycle life study of li-ion cells. J Power Sources 2001;101(2):238–47.
[44] Hall J, Schoen A, Allen P, Liu P, Kirby K. Resistance growth in lithium ion satellite cells. i. Non destructive data analyses. In: 208th ECS meeting. The Electrochemical Society; 2005. p. 242–242.
[45] Park CS. Fundamentals of engineering economics. Upper Saddle River, NJ: Pearson/Prentice Hall; 2004.
[46] IRENA. Renewable capacity statistics 2018. Tech. rep. International Renewable Energy Agency (IRENA), Abu Dhabi; 2018.
[47] Luque A, Hegedus S. Handbook of photovoltaic science and engineering. John Wiley & Sons; 2011.
[48] Branker K, Pathak M, Pearce JM. A review of solar photovoltaic levelized cost of electricity. Renew Sustain Energy Rev 2011;15(9):4470–82.
[49] Skoczek A, Sample T, Dunlop ED. The results of performance measurements of field-aged crystalline silicon photovoltaic modules. Prog Photovolt: Res Appl 2009;17(4):227–40.
[50] Time of use rate – Ontario Energy Board, (accessed on 2018-10-20). https://www.oeb.ca/rates-and-your-bill/electricity-rates/managing-costs-time-use-rates.
[51] Fu R, Feldman DJ, Margolis RM, Woodhouse MA, Ardani KB. Us solar photovoltaic system cost benchmark: Q1 2017. Tech. rep. Golden, CO (United States): National Renewable Energy Lab. (NREL); 2017.
[52] Kittner N, Lill F, Kammen DM. Energy storage deployment and innovation for the clean energy transition. Nat Energy 2017;2(9):17125.
[53] Temperature data. https://www.wunderground.com [accessed on 2018-10-20].
[54] El Amin I, Zia MF, Shafiullah M. Selecting energy storage systems with wind power in distribution network. IECON 2016-42nd annual conference of the IEEE Industrial Electronics Society. IEEE; 2016. p. 4229–34.
[55] Mohammed OH, Amirat Y, Benbouzid M, Feld G, Tang T, Elbast A. Optimal design of a stand-alone hybrid pv/fuel cell power system for the city of brest in France. Int J Energy Convers 2014;2(1):1–7.
[56] Irradiance data. http://www.solarelectricityhandbook.com/solar-irradiance.html [accessed on 2018-10-20].
[57] Li C, Chaudhary SK, Savaghebi M, Vasquez JC, Guerrero JM. Power flow analysis for low-voltage ac and dc microgrids considering droop control and virtual impedance. IEEE Trans Smart Grid 2017;8(6):2754–64.
[58] Beal L, Hill D, Martin R, Hedengren J. Gekko optimization suite. Processes 2018;6(8):106.
[59] Wächter A, Biegler LT. On the implementation of an interior-point filter line-search algorithm for large-scale nonlinear programming. Math Program 2006;106(1):25–57.
[60] Kim N, Rousseau A. Electric drive vehicle level control development under various thermal conditions: 2012 DOE hydrogen program and vehicle technologies annual merit review. Tech. rep. Virginia, US: Department of Energy; 2012.